

RESEARCH ARTICLE

10.1029/2019JA027346

This article is a companion to Breer et al. (2016), <https://doi.org/10.1029/2019JA027147>.

Key Points:

- Localized regions of stagnant flow are most indicative of the presence of a plume at Europa
- The visibility of plumes in spacecraft data highly depends on the density profile of the global atmosphere and the presence of an induced dipole
- Precise knowledge of the plasma's upstream parameters is required to identify plumes in spacecraft data

Correspondence to:

H. Arnold,
hannes.arnold@eas.gatech.edu

Citation:

Arnold, H., Liuzzo, L., & Simon, S. (2020). Plasma interaction signatures of plumes at Europa. *Journal of Geophysical Research: Space Physics*, 125, e2019JA027346. <https://doi.org/10.1029/2019JA027346>

Received 27 AUG 2019

Accepted 24 NOV 2019

Accepted article online 9 DEC 2019

Plasma Interaction Signatures of Plumes at Europa

Hannes Arnold¹, Lucas Liuzzo², and Sven Simon¹

¹School of Earth and Atmospheric Sciences, Georgia Institute of Technology, Atlanta, GA, USA, ²Space Sciences Laboratory, University of California, Berkeley, CA, USA

Abstract The goal of our study is to present a systematic modeling framework for the identification of water vapor plumes in plasma and magnetic field data from spacecraft flybys of Europa. In particular, we determine the degree to which different plume configurations can be obscured by the interaction of Jupiter's magnetospheric plasma with Europa's induced dipole field and its global atmosphere. We apply the hybrid model AIKEF (kinetic ions, fluid electrons) to investigate the effect of inhomogeneities in Europa's atmosphere (plumes) on the plasma interaction with the Jovian magnetosphere. To systematically assess the magnitude and structure of the perturbations associated with the plume-plasma interaction at Europa, we vary the plume location across Europa's surface while considering different symmetric and asymmetric density profiles of the moon's global atmosphere. To isolate the impact of a plume on Europa's magnetospheric environment, we also conduct model runs without any global atmosphere. To quantify the magnetic perturbations caused by plumes, we analyze the field components along hypothetical spacecraft trajectories through each plume. Conclusions of our study are (1) localized regions of stagnant flow are most indicative of the presence of a plume. (2) The visibility of plumes in the magnetic field strongly depends on the density profile (whether it is symmetric or asymmetric) of the global atmosphere. (3) The presence of an induced dipole complicates the identification of magnetic signatures associated with a plume and dominates Europa's magnetic environment in its intermediate vicinity. (4) Complex fine structures are visible in the tail of escaping plume ions.

1. Introduction

Europa (radius $R_E = 1,560.8$ km), Jupiter's innermost icy moon, orbits its parent planet at a distance of $9.38 R_J$ (radius of Jupiter $R_J = 71,492$ km) and is tidally locked to the planet. The moon is located within Jupiter's magnetosphere (Smith et al., 1974) and its plasma sheet (Kivelson et al., 2009). Europa's orbital period is significantly larger than Jupiter's rotational period, resulting in a synodic period of 11.23 hr with respect to Europa. Subsonic and subalfvénic magnetospheric plasma therefore continuously impinges onto the moon's atmosphere and ionosphere (Kivelson et al., 2004).

Impinging magnetospheric particles sputter molecules off Europa's icy surface, thereby generating a thin atmosphere that mostly consists of molecular oxygen O_2 (Burger & Johnson, 2004; Ip et al., 1998; McGrath & Hansen, 2009). The magnetospheric particle precipitation is not homogeneous but depends strongly on the orientation of the magnetospheric background field (Cassidy et al., 2013) and also, on the local electromagnetic field perturbations near Europa (Breer et al., 2019). The intensity of the sputtering decreases from Europa's ramside to its wake (Pospieszalska & Johnson, 1989), as the flux of the impinging magnetospheric particles is reduced in the moon's wakeside hemisphere (Cassidy et al., 2013). Yet the detailed understanding of the mechanisms responsible for the formation of Europa's O_2 atmosphere are still under heavy debate (Plainaki et al., 2018). The neutral atmosphere is partially ionized, mainly by electron impact ionization, with the contribution of solar ultraviolet (UV) ionization being an order of magnitude weaker (Saur et al., 1999). The large-scale asymmetries in the atmosphere are imprinted onto the shape of Europa's ionosphere.

The impinging magnetospheric plasma slows down in the vicinity of the moon due to mass loading from its ionosphere. Newly generated ionospheric ions are picked up by the ambient electromagnetic fields and are incorporated into the magnetospheric flow, causing a deceleration of the flow and an increase of the magnetic field strength upstream of the moon. The magnetospheric field drapes around the obstacle, generating Alfvén wings at larger distances to the moon which propagate northward and southward along the Alfvén characteristics $\vec{u}_0 \pm \vec{v}_{A0}$, where \vec{u}_0 is the bulk velocity of the magnetospheric upstream plasma and \vec{v}_{A0} is the Alfvén velocity (Neubauer, 1980, 1998). In addition to Europa's atmosphere and ionosphere, the

magnetospheric plasma interacts with the (time-varying) dipole field induced in the moon's subsurface ocean (Kivelson et al., 1999; Zimmer et al., 2000), which is driven by the 9.6° tilt between Jupiter's magnetic and rotational axes. This induced dipole field is compressed at Europa's ramside and stretched at its wakeside, locally contributing to transverse currents and therefore to the Alfvén wings (Liuzzo et al., 2016). The coupling of the dipole-magnetosphere interaction and the ionospheric mass loading reduces the cross section of the Alfvén wings and generates a slight displacement of the wings with respect to the moon (Neubauer, 1999; Volwerk et al., 2007).

However, the view of Europa's neutral gas environment was changed drastically when, in December 2012, Hubble Space Telescope (HST) observations of the moon's UV aurora revealed a localized surplus of UV emission intensity near its south pole, associated with an increase in oxygen and hydrogen column densities. Roth et al. (2014) showed that two water vapor plumes emanating near 180°W 75°S and 55°S, each with a scale height of about 200 km, quantitatively match the HST observations. Through image postprocessing, Sparks et al. (2016) found hints of additional transient plumes, located near the south pole at 271°W 63°S and in the equatorial region at 275.7°W 16.4°S. However, subsequent observations from HST could not identify the anomalies observed in 2012 (Roth et al., 2014, 2016).

Blöcker et al. (2016) used a three-dimensional magnetohydrodynamic model to investigate the detectability of a plume in Europa's magnetic environment. They showed that a plume in Europa's southern hemisphere generates a tube-like region of enhanced current density within the main southern Alfvén wing, called an *Alfvén winglet*. Like the main Alfvén wing, the winglet's current system will extend to arbitrarily large distances from Europa (due to the translational invariance of the Alfvén wing along its characteristics, see Neubauer, 1980) and may allow for a "remote" detection of plumes in magnetic field data from distant Europa flybys. Nevertheless, due to limitations of their model (e.g., the missing ionospheric Hall effect), Blöcker et al. (2016) were not able to present conclusive evidence for a plume crossing in magnetic field data from Galileo's flybys of Europa.

Only 2 out of 11 Galileo flybys passed Europa at a low altitude of just 400 km during closest approach, the E12 and E26 flybys (Kivelson et al., 2009). Magnetic field observations from both flybys show narrow, distinct perturbations in all three field components, as suggested by Blöcker et al. (2016) due to a potential Alfvén winglet. By using the BATS-R-US multifluid model, Jia et al. (2018) presented strong evidence for a plume near Europa's equator in magnetic field data from the E12 encounter on December 1997. These authors showed that the observed sharp drops and enhancements in all three magnetic field components are consistent with the spacecraft passing through a plume around closest approach. Additionally, they strengthened their hypothesis by matching the density enhancement observed by the Galileo Plasma Wave Spectrometer near closest approach (C/A). Arnold et al. (2019) presented evidence for plume activity in Europa's southern trailing hemisphere during Galileo's E26 flyby on 3 January 2000 by using the hybrid code AIKEF (Adaptive Ion-Kinetic Electron-Fluid, Müller et al., 2011). These authors showed that the fine structures in the draping signatures observed during E26 are not reproducible without taking into account a plume, whereas with the plume incorporated, numerous key features of the modeled magnetic field signatures are nearly indistinguishable from observations. Plumes at Europa therefore seem to have been a persistent phenomenon during the Galileo era.

Until now, plumes at Europa have been identified in plasma and magnetic field data only for two specific magnetospheric field orientations and plume locations. However, a systematic understanding of how the plume's location affects the plasma flow and magnetic field is still missing. Also, it is yet unclear to which degree the plasma interaction with the global atmosphere and the induced field can obscure the local interaction signatures of a plume at different locations. Our study therefore aims to systematically assess the magnitude and structure of the perturbations associated with plume-plasma interactions at Europa for various plume locations at the moon's surface and for different representations of the moon's global atmosphere. We will consider symmetric and asymmetric density profiles of Europa's neutral gas envelope. To isolate the impact of a plume on Europa's magnetospheric environment, we will also model Europa's plasma interaction without any global atmosphere. We will determine the degree to which different plume configurations can be obscured by the plasma interaction with Europa's induced dipole field and its global atmosphere. We note that due to their large closest approach altitudes, we do not expect to find new plume signatures in magnetic field data from flybys other than E12 and E26 (which have already been studied).

Table 1
The Plasma, Atmosphere, and Plume Parameters of the Simulation Runs

Scenario	Upstream plasma				Global Atmosphere			Plume					
	\vec{B}_0 (nT)	u_0 (km/s)	n (m^{-3})	$kT_i = kT_e$ (eV)	n_0 (m^{-3})	h_0 (km)	A	$n_{p,0}$ (m^{-3})	h_p (km)	$\Delta\theta$ [$^\circ$]	θ_F ($^\circ$)	ϕ_F ($^\circ$)	$kT_{\text{H}_2\text{O}}$ (eV)
#U.1	(0,0,-450)	100	$60 \cdot 10^6$	100	—	—	—	$3.9 \cdot 10^{15}$	200	15	90	270	0.1
#U.2	(0,0,-450)	100	$60 \cdot 10^6$	100	$5 \cdot 10^{13}$	100	0	$3.9 \cdot 10^{15}$	200	15	90	270	0.1
#U.3	(0,0,-450)	100	$60 \cdot 10^6$	100	$5 \cdot 10^{13}$	100	10	$3.9 \cdot 10^{15}$	200	15	90	270	0.1
#U.4	(0,-210,-450)	100	$60 \cdot 10^6$	100	$5 \cdot 10^{13}$	100	10	$3.9 \cdot 10^{15}$	200	15	90	270	0.1
#S.1	(0,0,-450)	100	$60 \cdot 10^6$	100	—	—	—	$3.9 \cdot 10^{15}$	200	15	180	0	0.1
#S.2	(0,0,-450)	100	$60 \cdot 10^6$	100	$5 \cdot 10^{13}$	100	0	$3.9 \cdot 10^{15}$	200	15	180	0	0.1
#S.3	(0,0,-450)	100	$60 \cdot 10^6$	100	$5 \cdot 10^{13}$	100	10	$3.9 \cdot 10^{15}$	200	15	180	0	0.1
#S.4	(0,-210,-450)	100	$60 \cdot 10^6$	100	$5 \cdot 10^{13}$	100	10	$3.9 \cdot 10^{15}$	200	15	180	0	0.1
#D.1	(0,0,-450)	100	$60 \cdot 10^6$	100	—	—	—	$3.9 \cdot 10^{15}$	200	15	90	90	0.1
#D.2	(0,0,-450)	100	$60 \cdot 10^6$	100	$5 \cdot 10^{13}$	100	0	$3.9 \cdot 10^{15}$	200	15	90	90	0.1
#D.3	(0,0,-450)	100	$60 \cdot 10^6$	100	$5 \cdot 10^{13}$	100	10	$3.9 \cdot 10^{15}$	200	15	90	90	0.1
#D.4	(0,-210,-450)	100	$60 \cdot 10^6$	100	$5 \cdot 10^{13}$	100	10	$3.9 \cdot 10^{15}$	200	15	90	90	0.1
#JA	(0,0,-450)	100	$60 \cdot 10^6$	100	$5 \cdot 10^{13}$	100	0	—	—	—	—	—	—

Note. The symbols in the first column denote the “ingredients” of each model scenario: “U” (upstream, referring to a plume located at $(r, \theta_F, \phi_F) = (R_E, 90^\circ, 270^\circ)$), “S” (south pole, a plume located at $(r, \theta_F, \phi_F) = (R_E, 180^\circ, 0^\circ)$), and “D” (downstream, a plume at $(r, \theta_F, \phi_F) = (R_E, 90^\circ, 90^\circ)$). For each model setup, runs ending with “.1” denote the case without any global atmosphere at all, whereas “.2” and “.3” stand for the case with a symmetric and asymmetric global atmosphere, respectively. Runs ending with “.4” consider the plasma interaction with a local plume source, Europa’s asymmetric global atmosphere and a induced dipolar field from the moon’s subsurface ocean. All other symbols from the table are defined in the text. The final run (labeled JA) considers only a symmetric global atmosphere, but no plume source at all.

The structure of the paper is as follows: In section 2 a description of the simulation model and the model parameters are given. Section 3 presents and discusses the results of our study. Section 4 concludes the paper with a summary of our findings.

2. Model Description

To model Europa’s interaction with its magnetospheric environment, we use the AIKEF (Adaptive Ion-Kinetic Electron-Fluid) hybrid code (Müller et al., 2011), which treats ions as particles and electrons as a massless, charge-neutralizing fluid. Therefore, our model can describe the flow shear between the magnetospheric plasma and ionospheric particles emanating from Europa, as well as the ionospheric Hall effect. The results of Blöcker et al. (2016) and Jia et al. (2018) indicate that any reasonable model of plume-plasma interactions at Europa should take into account the Hall effect within the plumes. The AIKEF code has already been successfully applied to study plume-plasma interactions at Europa during the Galileo E26 flyby (Arnold et al., 2019). Previously, the code has been used to model Cassini magnetic field observations from multiple flybys through the Enceladus plume (Kriegel et al., 2009, 2011, 2014) and also to study the plasma interaction of Callisto, another Galilean moon of Jupiter (Liuzzo et al., 2015, 2016, 2017, 2018). In addition, AIKEF has been successfully applied to, for example, Titan (Feyerabend et al., 2015, 2016) and Mercury (Müller et al., 2012).

In our model we use the EPhiO coordinate system. It is a Cartesian coordinate system, where the x axis is aligned with the corotational flow direction, the y axis points toward Jupiter, and the z axis completes the right-handed system. The origin of the EPhiO system is located at the center of Europa. The spherical coordinate system (r, θ, ϕ) associated with the EPhiO coordinate system is described by the radius r , the latitude θ measured from the positive z axis, and ϕ denotes west longitude measured clockwise from the positive y axis. The parameters for our simulations can be found in Table 1. Parameters are categorized in values for the upstream plasma, global atmosphere, and plume. For each of our simulations, the plume is either located at the apex of the trailing hemisphere (upstream “U,” in spherical EPhiO coordinates, $(r, \theta_F, \phi_F) = (R_E, 90^\circ, 270^\circ)$), the apex of the leading hemisphere (downstream “D,” $(r, \theta_F, \phi_F) = (R_E, 90^\circ, 90^\circ)$), or at Europa’s south pole (“S,” $(r, \theta_F, \phi_F) = (R_E, 180^\circ, 0^\circ)$), as seen in Figure 1. At all three locations, the plume axis is oriented perpendicular to Europa’s surface. By choosing these locations, we keep the geometry of the interaction scenario as simple as possible, while the locations of the plume foot points are still similar to observations by

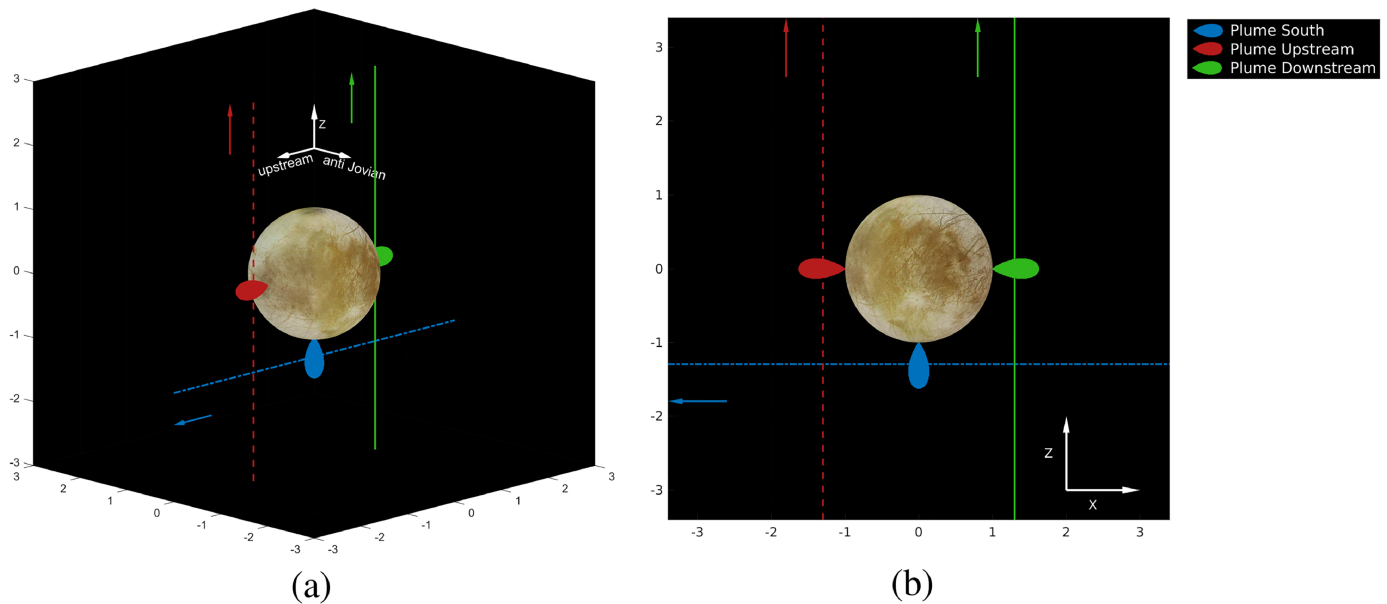


Figure 1. Geometry of the three plume locations analyzed in this work as well as the synthetic trajectories used to study the magnetic signatures of these plumes (see section 3.5). In panel (a), the view point is located upstream, from the Jupiter-averted side, whereas in panel (b) we see Europa from the viewing angles $(\theta, \phi) = (180^\circ, 90^\circ)$. The dotted, red line represents a (hypothetical) flyby through a plume located upstream ($x = -1.3 R_E$, $y = 0$ and z varying), the blue line depicts a crossing of a south polar plume (x varying, $y = 0$ and $z = -1.3 R_E$), and the green line corresponds to a flyby through a plume located at Europa's leading/downstream apex ($x = 1.3 R_E$, $y = 0$ and z varying), respectively.

HST (similar to the south polar foot point of Roth et al., 2014 and the equatorial foot point of Sparks et al., 2016). For each of these three plume locations, a series of four simulation runs has been carried out: Runs denoted by label “.1” do not consider any global atmosphere at all; that is, the incident plasma interacts with the plume or directly with Europa's absorbing surface. The goal of these runs is to define a “baseline” for subsequent studies of the obstruction of a plume by an atmosphere (of varying complexity) and an induced dipole. For each plume configuration, runs denoted by “.2” and “.3” take into account a global symmetric or asymmetric atmosphere, respectively. Even though the asymmetric model for the atmosphere seems to be closer to reality (Cassidy et al., 2013; Plainaki et al., 2018; Rubin et al., 2015), the simulations with a symmetric atmosphere facilitate a discrimination between asymmetries in the plasma interaction generated by the global atmosphere or by the location of the plume source. Runs labeled “.4” consider the plasma interaction with a plume source, Europa's asymmetric global atmosphere and an induced dipolar field from the moon's subsurface ocean. This is the most realistic scenario and will be likely observed during flybys (e.g., Arnold et al., 2019; Jia et al., 2018).

To facilitate a comparison to previous results (e.g., to Blöcker et al., 2016, and Arnold et al., 2019), we apply a similar set of parameters for the upstream plasma. The value for the bulk velocity of the (partially) corotating plasma is $u_0 = 100$ km/s, which is in agreement with Kivelson et al. (2009), Bagenal et al. (2015). The upstream number density in our model, $n = 60 \cdot 10^6 \text{ m}^{-3}$, is within the range measured during various Galileo flybys (Kivelson et al., 2004; Kurth et al., 2001). Although the incident plasma parameters depend on Europa's distance to the Jovian current sheet, the Alfvénic Mach number M_A remains always $\ll 1$; that is, the key features of the interaction change only quantitatively, but not qualitatively (Kivelson et al., 2009). The mass of the singly charged upstream ions is set to $m_i = 18.5$ amu, and the ion and electron temperatures read $k_B T_i = k_B T_e = 100$ eV (Kivelson et al., 2004). We set the magnetospheric background field to $\vec{B}_0 = (0, 0, -450)$ nT for the Simulation Runs “.1” to “.3,” similar to Blöcker et al. (2016). This orientation and strength of the field are consistent with measurements taken when Europa was located close the center of Jupiter's magnetospheric current sheet (Kivelson et al., 1999). The scenario of Runs “.4,” where the external magnetospheric field is set to $\vec{B}_0 = (0, -210, -450)$ nT, corresponds to Europa being located north of the magnetospheric current sheet, where the field also has a radial component. The corotation-aligned component of the background field along Europa's orbit is usually negligible (see, e.g., Arnold et al., 2019; Kivelson et al. (1999)). By treating the subsurface ocean as a highly conducting medium, the induced magnetic moment

can be written as

$$\vec{M}_{ind} = -\frac{2\pi R_E^3}{\mu_0} (B_{x,0}\vec{x} + B_{y,0}\vec{y}), \quad (1)$$

where $B_{x,0}$ and $B_{y,0}$ are the components of the background magnetic field vector $\vec{B}_0 = B_{x,0}\vec{x} + B_{y,0}\vec{y} + B_{z,0}\vec{z}$ and \vec{x} , \vec{y} , \vec{z} denote the unit vectors of the EPhiO system (see Kivelson et al., 1999; Liuzzo et al., 2016; Zimmer et al., 2000). Thus, the induced magnetic field is absent in Runs “.1” to “.3,” whereas the slight change in the orientation of \vec{B}_0 for Run “.4” generates an induced magnetic moment that is aligned with the y axis. The parameters for all runs result in a plasma beta of $\beta \approx 0.01$, Alfvénic Mach number of $M_A \approx 0.3$ and a magnetosonic Mach number of $M_{MS} \approx 0.3$.

In our model, Europa’s global atmosphere consists of molecular oxygen, which is in agreement with observations (Hall et al., 1995; McGrath & Hansen, 2009). Pospieszalska and Johnson (1989) and Cassidy et al. (2013) have shown that the surface sputtering, and therefore, the distribution of neutral gas is not uniform at Europa. The sputtering rate was found to decrease from the trailing toward the leading hemisphere. Similar to Rubin et al. (2015), Jia et al. (2018), and Arnold et al. (2019), these asymmetries are taken into account by our model through the following density profile for the neutral gas:

$$\begin{aligned} n_L(h) &= n_0 \cdot \exp\left(-\frac{h}{h_0}\right), & 90^\circ < \alpha \leq 180^\circ, \\ n_T(h, \alpha) &= n_L(h) \cdot (1 + A \cdot \cos(\alpha)), & \alpha \leq 90^\circ, \end{aligned} \quad (2)$$

where n_T is the density profile in the trailing ($x < 0$) and n_L the profile in the leading hemisphere ($x > 0$). The symbol n_0 represents the density at the surface, h the radial distance $h = |\vec{r}| - R_E$ (where \vec{r} is the position vector from Europa’s center in EPhiO coordinates) to Europa’s surface, and h_0 the neutral scale height. The angle α is measured from the negative x axis and denotes the angle between the upstream direction ($-x$ axis) and the position vector \vec{r} . Therefore, α ranges from 0° to 180° . Thus, the model atmosphere exhibits rotational symmetry around the x axis; that is, the isolines of the atmospheric neutral density are circles around the x axis. The asymmetry between leading and trailing hemisphere is controlled through the parameter A , where $A = 0$ results in a symmetric (Runs “.2”) and $A = 10$ (adopted from Arnold et al., 2019) in an asymmetric density distribution (Runs “.3” and “.4”). In agreement with the model of Arnold et al. (2019) and HST observations (Hall et al., 1995; Plainaki et al., 2018; Saur et al., 1998), we have chosen a neutral scale height of $h_0 = 100$ km and a surface density of $n_0 = 5 \cdot 10^{13} \text{ m}^{-3}$.

To model a water vapor plume at Europa’s surface, we use a neutral density profile similar to Jia et al. (2018) and Arnold et al. (2019):

$$n_p(h, \Delta\theta) = n_{p,0} \cdot \exp\left[-\left(\frac{h}{h_p}\right)^2 - \left(\frac{\Delta\theta}{h_\theta}\right)^2\right], \quad (3)$$

where $n_{p,0}$ is the plume’s density at its foot point on Europa’s surface, h_p the scale height, and $2 \cdot h_\theta$ the opening angle of the plume. The parameter $\Delta\theta$ represents the angular distance from the center of the plume axis. The “origin” for the definition of $\Delta\theta$ is located at the foot point of the plume and *not* at the center of Europa. In contrast to Jia et al. (2018) and Arnold et al. (2019) the plume axis is perpendicular to Europa’s surface at all three plume locations. Since we aim to understand the general physics of plume-plasma interactions at Europa instead of analyzing a specific flyby data set, this approach facilitates straightforward access to the involved mechanisms. Again, to facilitate a comparison to Jia et al. (2018) and Arnold et al. (2019), we have chosen similar parameters, $h_p = 200$ km, $h_\theta = 15^\circ$ and $n_{p,0} = 3.9 \cdot 10^{15} \text{ m}^{-3}$, resulting in column densities of the plume similar to those observed by HST (Roth et al., 2014; Sparks et al., 2016).

Europa’s neutral gas envelope is partially ionized by electron impact ionization, which is an order of magnitude stronger than photoionization (Saur et al., 1998). In analogy to Schilling et al. (2008), Blöcker et al. (2016), Jia et al. (2018), and Arnold et al. (2019), we obtain the ion production rate by multiplying the electron impact ionization rate $f_{imp}(T_e)$ for H_2O and O_2 with the respective neutral density profile. The loss process included for the ionized molecules is dissociative recombination, which is several orders of magnitude weaker than ionization (Arnold et al., 2019; Jia et al., 2018). The generated ions are H_2O^+ from the plume and O_2^+ from the global atmosphere, respectively. We note that the mass-to-charge ratio of H_2O^+ is representative for the entire range of water group ion species. These ions are referred to as “plume” ions in

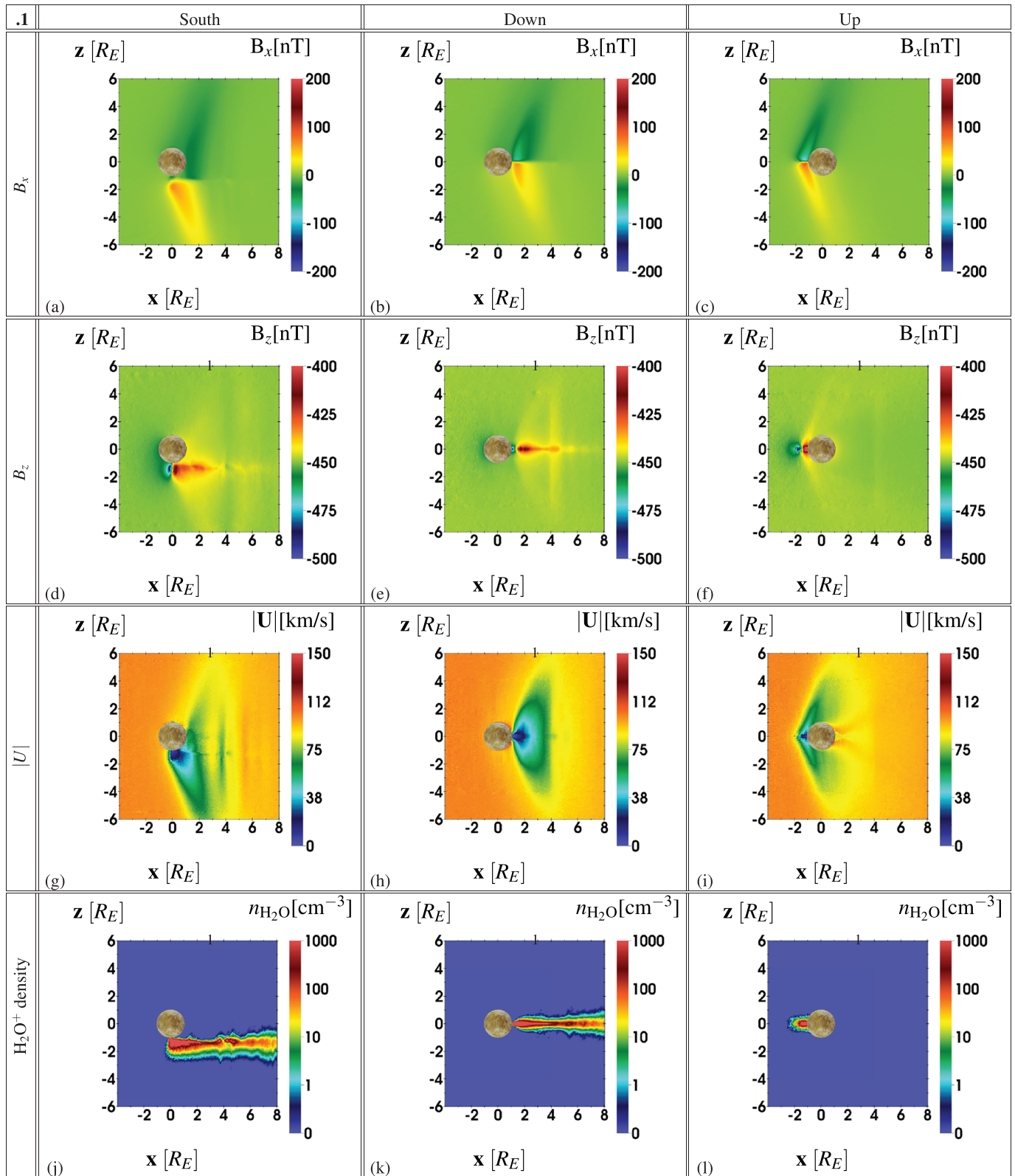


Figure 2. Two-dimensional cuts through the AIKEF simulation domain in the $y = 0$ plane, showing the B_x and B_z components (first and second row), as well as the bulk velocity of the plasma (third row) and the plume ion density (fourth row) for runs of Configuration “.1” (without any global atmosphere). For the runs in the first column, the plume is located at Europa’s south pole (“S”), whereas in the second and third columns the plume is located at the downstream (“D”) and upstream (“U”) apices, respectively (see section 2 for details).

the following. For a detailed description of the ionization model and the applied values of ionization/loss rates, we refer the reader to section 2 of Arnold et al. (2019).

The extension of the simulation domain is $-10 R_E \leq x \leq 20 R_E$, $-15 R_E \leq y \leq 15 R_E$, and $-30 R_E \leq z \leq 30 R_E$. The simulation grid contains two refinement levels centered around (0,0,0): The grid resolution is 33 km for $|x, y, z| \leq 1.5 R_E$, 66 km for $1.5 R_E < |x, y, z| \leq 3 R_E$, and 132 km at larger distances. The simulations reach stationarity after a passage of the plasma flow through the simulation domain.

To quantify the magnetic field perturbations caused by plumes at different surface locations, we analyze all three magnetic field components B_x , B_y , and B_z , along a hypothetical spacecraft trajectory through each plume (see Figure 1). Similar to the Galileo E12 and E26 flybys, we have chosen a closest approach altitude of $0.3 R_E$ and keep the flyby geometries simple, by varying only one coordinate along each trajectory (x for the south polar plume and z for the plumes located at the upstream and downstream apices). To assess the plume's imprint on the magnetic field along a given spacecraft trajectory, we conducted an additional series of runs "JA" (just atmosphere), with just a symmetric atmosphere ($A = 0$, *without a plume*); see section 3.5.

3. Results

3.1. Case 1: Plasma Interaction With a Plume and Europa's Solid Body

In Figures 2a–2c the B_x component of the magnetic field for Runs "1" (without a global atmosphere) is shown. Figure 2a corresponds to the scenario where the plume is located at Europa's south pole ("S"). In this scenario mass loading through ionization of plume neutrals results in an Alfvén wing in Europa's southern hemisphere. Due to hemisphere coupling between Europa's southern and northern hemisphere (Saur et al., 2007), there is a weak ($B_x \approx 2\%B_0$, where B_0 is the magnetospheric background field) draping signature visible in Europa's northern hemisphere and in its intermediate wake (within $2.5 R_E$). A similar effect was observed at Enceladus by the Cassini spacecraft (Simon et al., 2011; Simon et al., 2014). In Figure 2b (plume located at "D") and Figure 2c (plume located at "U") a narrow Alfvén wing forms at the plume's location, resulting in a wing downstream in Figure 2b and upstream in Figure 2c, respectively. However, the solid body of the moon itself does not impose any discernible draping on the magnetic field lines. As can be seen from Figures 2b and 2c, the B_x perturbations "above" and "below" Europa are practically zero. In principle, a plasma-absorbing moon (without any atmosphere) still generates a weak Alfvén wing, as shown by Simon et al. (2012) for Rhea. However, the intensity of the associated B_x perturbations is proportional to $1/B_0$. Due to the strong background field at Europa (more than a factor of 20 stronger than at Rhea), this effect does not make any discernible contribution to the field perturbations in Figures 2b and 2c. Ionized particles from a plume located at the upstream apex are transported toward Europa because of the $\vec{E} \times \vec{B}$ drift; that is, the flow of picked-up ions "overlaps" with the ion population within the plume. This effect results in a higher ion density in the plume for Case "U," compared to Case "D." This is also visible in the strength of the B_x perturbations (≈ 20 nT stronger in Case "U" than in Case "D").

Figures 2d–2f show the B_z component of the magnetic field. In the case of a south polar plume, a localized pileup of 25 nT in front of the plume can be observed. In contrast to this, the field lines pass through Europa's solid body unimpeded; that is, no discernible pileup is formed in front of the moon itself. In Figure 2e the pileup structure of the plume forms at Europa's wakeside, where the magnetospheric field lines reenter the plasma after diffusing through the moon's solid body and encounter the narrow tail of slow plume plasma (with same magnitude as in Case "S"). In Figure 2f the plume obstacle is encountered by the incident plasma before it even reaches Europa's surface, resulting in a localized, narrow pileup structure (of 0.5 – $1 R_E$ width) in front of the moon. In all three cases, the extension of the pileup is determined by the size of the plume and *not* by the diameter of Europa.

The bulk velocity $|\vec{U}|$ in Figures 2g–2i reveals the locations of the plumes, through slowing of the upstream plasma due to mass loading by the plume particles. These panels also show that the region where the plasma flow is decelerated by mass loading to $|\vec{U}| \leq 0.1U_0$ is much larger than the region where $|B_z|$ differs significantly from the background value of 450 nT. For a plume located at Europa's south pole or at the wakeside, the extension of this region is comparable to that of Europa. This results in an asymmetry between the plasma flow in the northern and southern hemispheres in the case of a south polar plume, as shown in Figure 2g. Thus, the electric field and the associated velocity of the pick-up ions are smaller in the southern than in the northern hemisphere. In the case of a plume located at the downstream or upstream apex, the perturbations in the velocity (and all other quantities) are symmetric between both hemispheres, as shown,

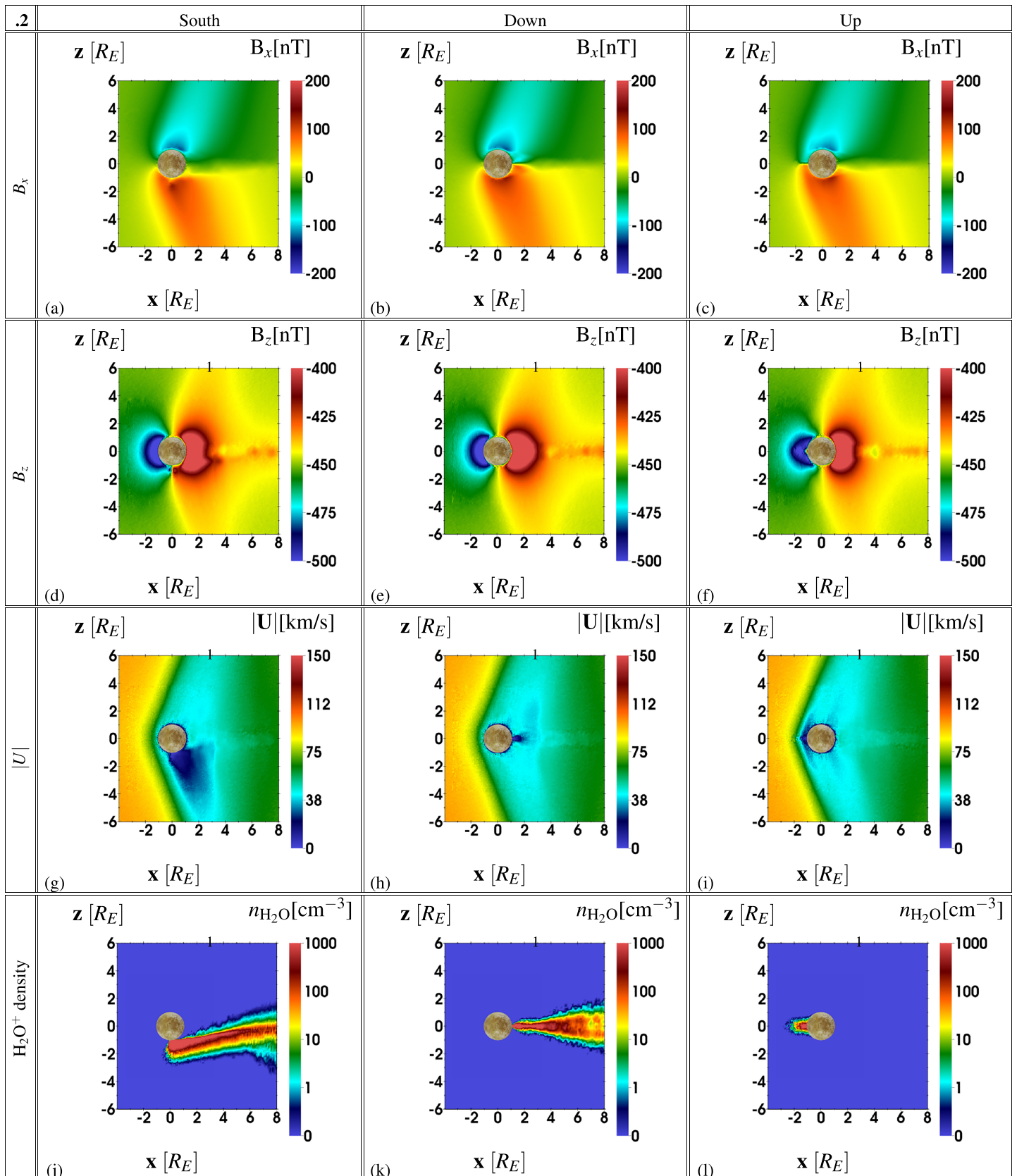


Figure 3. Two-dimensional cuts through the AIKEF simulation domain in the $y = 0$ plane for runs of configuration “.2.” The quantities shown in the panels are the same as in Figure 2.

for example, in Figures 2h and 2i. This is the result of the plume axis being located in the $z = 0$ plane and the symmetric Alfvén wave propagation perpendicular to that plane (due to the chosen orientation of \vec{B}_0).

The plume ion density is depicted in Figures 2j–2l. For a plume located at the upstream apex (Figure 2l), plume ions are confined to a pillar-like region ($\approx 1.5 R_E$ in length and width) upstream of Europa. There is no pick-up tail in Europa's wakeside hemisphere, since plasma produced through ionization of water vapor immediately reencounters Europa's surface and is unable to flow around the moon. The reason is the small extent (opening angle: $h_\theta = 15^\circ$) of the plume, compared to the size of the moon, which is a major difference to the Enceladus plume. The width of the pick-up tail (in z direction) in Figure 2j is determined by the scale height of the plume (since the plume axis is perpendicular to the upstream flow), whereas in Figure 2k the plume axis is aligned with the upstream flow, and therefore, the width of the tail is determined by the opening angle of the plume.

3.2. Case 2: Plasma Interaction With a Plume and a Symmetric Global Atmosphere at Europa

In Figures 3a–3c the B_x component of the magnetic field for Runs “.2” (with a global, symmetric atmosphere) is shown. In these runs, the overall plasma interaction is mainly driven by the mass loading from the global atmosphere, rather than the mass loading from the local plume source. This results in a modeled draping signature of $|B_x| \approx 150$ nT, which is an order of magnitude stronger than the draping in Series “.1” (see Figure 2), where the global atmosphere was not yet considered. The diameter of the Alfvén wings, mainly driven by the atmosphere, is now comparable to the size of the Europa obstacle (Figures 3a–3c). The magnitude of magnetic pileup (visible in the B_z component, see Figures 3d–3f) upstream of the obstacle is of the same order as the pileup due to a plume alone (see Figures 2d–2f) but much more extended. Thus, the plume signature in B_z is almost completely “buried” within this extended pileup region. Nonetheless, the plumes in all three scenarios are still visible in the fine structures of the magnetic field. In Figure 3a we see a localized (within $0.5 R_E$ from the surface) enhancement of the draping below Europa's south pole (depicted in dark red), compared to the rather uniform B_x perturbations above the moon's north pole. Additionally, Figures 3d and 3f reveal a highly localized pileup in front of the plume's location (within $0.5 R_E$, depicted in dark blue), whereas Figure 3e shows no plume signature at all and the plume completely “disappears” in the magnetic depletion region downstream of Europa (dark red). Hence, the inclusion of a global atmosphere obscures large portions of the magnetic signatures generated by a plume source alone.

The plasma quantity that is again most indicative of a plume is the bulk velocity $|\vec{U}|$ (Figures 3g–3i). When a global atmosphere is included, the deceleration of the flow due to the mass loading is much more pronounced than in Figure 2: The plasma flow within the Alfvén wing tubes is slowed down to below 40 km/s. In Case “.1” such a strong deceleration occurs only in the immediate vicinity of the plume. In Case “.2,” the region of decelerated flow extends to Europa's wakeside (up to several Earth radii in the x direction). Again, this region is symmetric between the moon's northern and southern hemispheres for a plume located at “U” and “D.” For a plume located at the south pole, the region of nearly stagnating flow still possesses a pronounced north-south asymmetry (see Figure 3g) that should be detectable by a spacecraft, despite the superimposed reduction in flow speed caused by Europa's global atmosphere.

The plume ion density is depicted in Figures 3j–3l. In the case of a plume at Europa's south pole (Figure 3j), the pick-up tail is slightly inclined northward due to the $\vec{E} \times \vec{B}$ drift perpendicular to the draped magnetic field lines. At larger distances along the corotation direction, where the field lines straighten again, the tail becomes more aligned with the x axis. This tilt of the pick-up tail is not visible in runs of Series “.1” (without a global atmosphere) because the mass loading and therefore, the draping of the magnetic field lines is significantly weaker. In the case of a plume at Europa's downstream apex, the pick-up tail is again symmetric between the northern and southern hemispheres (Figure 3k). We note that this symmetry is also partially caused by the chosen orientation of the background field (in negative z direction) and would disappear, if Europa were placed outside of the Jovian magnetospheric current sheet (see Case “.4,” visible in Figure 3k). For a plume located at Europa's downstream apex, the pick-up ions tend to “refill” the region of reduced magnetic field in Europa's geometric plasma shadow, which results in a broadening of the pick-up tail. For a plume located upstream, again, no pick-up tail is visible at Europa's wakeside, because newly generated ions immediately “rain” down onto the moon.

The mass of plume ions is much lower than the mass of exospheric O_2^+ pick-up ions. Therefore, the ray-like density enhancement associated with the plume should be clearly discernible in spacecraft data. Also, plume ions (H_2O^+) would generate pick-up waves at a significantly higher frequency than exospheric O_2^+ (≈ 2 times

higher, due to the mass difference between the species), thus being visible in magnetic field data (Desai et al., 2017; Volwerk et al., 2001).

3.3. Case 3: Plasma Interaction With a Plume and an Asymmetric Global Atmosphere at Europa

In Figures 4a–4f the magnetic field components for the plasma interaction with a plume and an asymmetric global atmosphere are shown. The most prominent effect of a ram-wake asymmetry in the global atmosphere is visible in the B_x component (Figures 4a–4c). Whereas the B_x signature in Case “.2” is nearly homogeneous across Europa’s north and south polar caps (in Cases “U” and “D”), in Scenario “.3,” $|B_x|$ is stronger by ≈ 50 nT at Europa’s ramside. This enhancement is generated by the increased mass loading due to a thicker neutral atmosphere around Europa’s ramside apex (due to the asymmetry factor $A = 10$ in equation (2)). Similar to Case “.2,” the plume causes additional perturbations of only a few nanoteslas in its immediate vicinity, whereas the Alfvén winglet at larger distances is barely visible within the “main” wing generated by the global atmosphere. In B_z (Figures 4d–4f), subtle changes due to inclusion of global asymmetries in the atmosphere now “compete” with the signatures of a local plume source. For the run with a south polar plume, the plume location coincides with the transition from the angle-dependent to the radially symmetric neutral gas profile (see equation (2)). Therefore, while the plume still generates a distinct “kink” in the B_z component below Europa’s south pole, the separate pileup feature in front of the plume has vanished (see Figure 4d). For the case of a plume located at Europa’s ramside, the associated pileup is completely obscured by the magnetic signatures of the enhanced neutral density of the global atmosphere (see Figure 4f). For the plume located at Europa’s wakeside apex, the plume signature remains buried within the mass loading signatures of Europa’s global atmosphere, similar to Case “.2.”

The localized drop in the plasma’s bulk velocity (Figures 4g–4i) is again most indicative for the presence of a plume. However, compared to Case “.2,” shape and strength of the flow deceleration are nearly unaffected by inclusion of global asymmetries in the atmosphere. The enhanced neutral densities in Case “.3” are confined to Europa’s ramside hemisphere. Hence, many newly generated ions from the “surplus” of neutral gas immediately reencounter the moon and are absorbed, rather than contributing to mass loading and pick-up (similar to the plume ions in the “U” scenarios). Therefore, the effect of the enhanced atmospheric ramside density on the flow is rather subtle. The shape of the plume’s pick-up tail (Figures 4j–4l) is nearly unaffected by the asymmetry in Europa’s global atmosphere. Only the width of the plume’s pick-up tail is slightly broader in Case “.2” than in Case “.3” (see Figures 3 and 4). These subtle differences are caused by the slightly stronger deflection of the upstream plasma in the case of an asymmetric atmosphere, which also affects the fields and flow pattern downstream of Europa.

3.4. Case 4: Plasma Interaction With a Plume, Induced Dipole, and an Asymmetric Global Atmosphere at Europa

Figures 5a–5c show the B_x component for Case “.4,” the plasma interaction with a plume, induced dipole and an asymmetric global atmosphere. Due to $B_{y,0}$ being nonzero, the Alfvén wing characteristics are no longer parallel to any plane of the EPHIO system. Therefore, for a better understanding of the involved physics we display the plasma interaction signatures in a rotated system (x, \bar{y}, \bar{z}) such that the (x, \bar{z}) plane contains the wing characteristics. The rotation angle α around the x axis is $\alpha = \arctan(B_{y,0}/B_{z,0}) = 25^\circ$. The magnetic field orientation in Case “.4” results in a highly complex geometry for the case of a south polar plume, where the plume axis is no longer contained within any of the coordinate planes. Therefore, we subsequently study the magnetic field along hypothetical trajectories to better understand the local influence of the plume.

The diameter of the Alfvén wings is visibly shrunk compared to Cases “.2” and “.3” (less than $2 R_E$ compared to $3 R_E$), due to the local twist of \vec{B} caused in the immediate vicinity of Europa by the induced dipole. This shrinkage has been theoretically predicted by Neubauer (1999), and it was observed at Europa by Galileo, for example, during the E26 flyby (Volwerk et al., 2007). Without any plasma effects the induced dipole field would generate a shamrock-like structure in the B_x component (see Liuzzo et al., 2016 for a detailed discussion). In Figures 5b and 5c these “shamrock leaves” are still discernible at Europa’s wakeside ($B_x > 0$ for $\bar{z} > 0$ and $B_x < 0$ for $\bar{z} < 0$), albeit being compressed by the Alfvén wings. In the case of a south polar plume (Figure 5a), asymmetric draping near the plume’s location is visible. For a plume at Europa’s wakeside, the signature of the two B_x “leaves” in Europa’s downstream hemisphere is amplified (see Figure 5b). The “leaf”-like structure in Europa’s wake gets compressed by the Alfvén wings from the “outside” and by the plume located in between the two regions of opposite B_x polarity. A plume located at Europa’s ramside apex counteracts the compression of the dipole and leads to a small extension of the field line draping

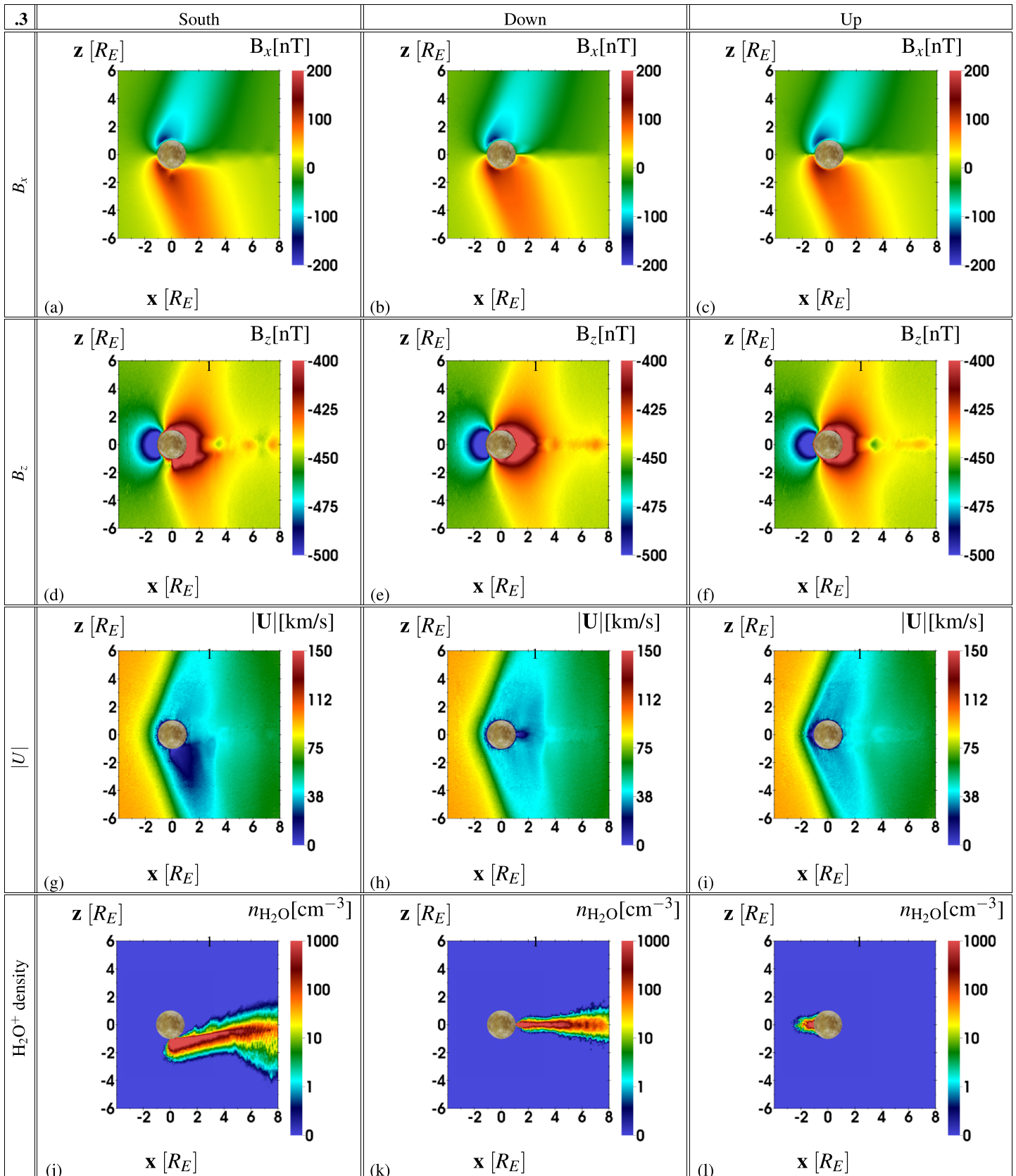


Figure 4. Two-dimensional cuts through the AIKEF simulation domain in the $y = 0$ plane for runs of Configuration “.3.” The quantities shown in the panels are the same as in Figures 2 and 3.

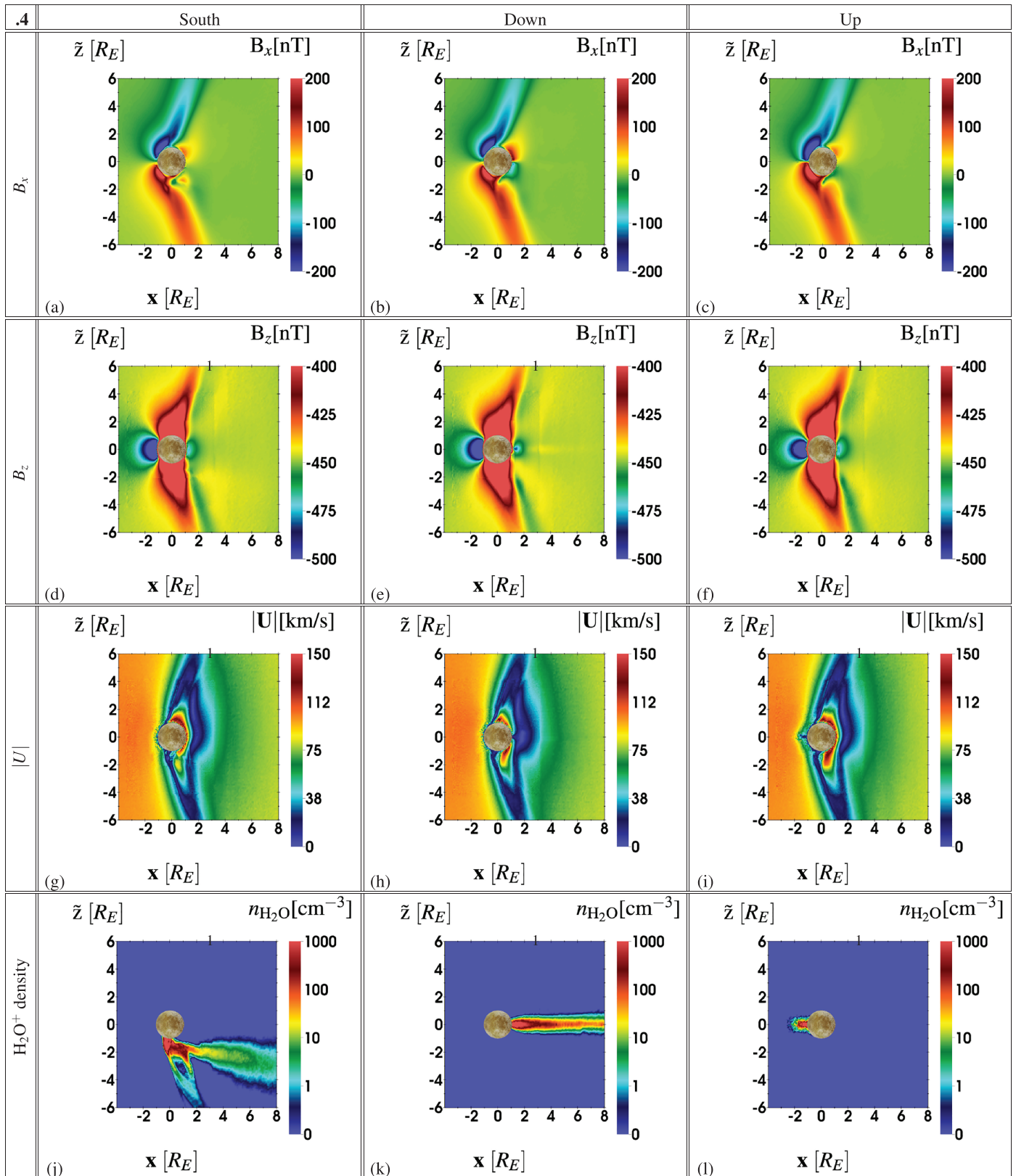


Figure 5. Two-dimensional cuts through the AIKEF simulation domain for Case “.4,” where \tilde{z} is rotated around the x axis by the angle $\alpha_z = \arctan(B_{y,0}/B_{z,0}) \approx 25^\circ$, therefore showing the interaction region in the plane which contains the Alfvén characteristics $\tilde{v}_{a0} \pm \tilde{u}_0$ and the upstream flow velocity \tilde{u}_0 . The quantities shown in the panels are the same as in Figures 2–4.

($1 R_E$). Overall, due to the more compact structure of the Alfvén wings, the Alfvén winglet in B_x (visible in Cases “.1” to “.3,” see Figures 2–4) is not discernible over the “main” wing any more. This finding is also true for cutting planes other than the (x, \bar{y}, \bar{z}) plane shown in Figure 5. The B_z component (Figures 5d–5f) shows only minor quantitative differences between the three plume locations. The pileup structure in front of the plume is now completely buried within the signatures generated by the plasma interaction with the atmosphere and induced dipole. In other words, considering the induced dipole eliminates most of the signatures associated with a plume in Scenarios “.1” to “.3.” Therefore, a flyby that is most “suitable” for the identification of plumes in magnetic field data should take place with Europa located close to the center of the Jovian current sheet (our Cases 2–3), where the induced dipole is weak or even vanishes (Zimmer et al., 2000).

The bulk velocity $|\vec{U}|$ (Figures 5g–5i) no longer shows a distinct region (with a similar size as Europa) of reduced momentum due to mass loading by the plume plasma (in contrast to Cases “.1” to “.3”). The induced dipole increases the strength of the obstacle to the plasma flow and reduces the plasma bulk velocity to below 20 km/s within the entire Alfvén wing (compared to ≈ 40 km/s in the cases without a dipole). Due to the tilt of the plume axis in Scenario “S” (out of the $x - \bar{z}$ plane), the plasma is already reaccelerated at the flanks of the plume (resulting in the yellow region directly below the south pole in Figure 5g). For a plume located at Europa’s ramside apex, upstream flow stagnation associated with the plume is visible in a ray-like region (see Figure 5i). Overall, the plume signature with a dipole included is barely noticeable in the bulk velocity (on length scales of $\leq 1 R_E$).

In Figure 5j, where the south polar plume axis is inclined against both, the background magnetic field and the induced dipole, our model reveals a complex, three-dimensional outflow pattern with several ray-like regions of enhanced ion density. Such a filamentation of the pick-up tail has been observed by Cassini at Titan (Coates et al., 2012) and also occurs in hybrid simulations of the Titan interaction (Feyerabend et al., 2015). For plumes located at Europa’s ramside (see Figure 5l) or wakeside (see Figure 5k), the geometry of the pick-up ion tail does not change compared to Cases “.1 to .3.”

In our hybrid model results, the obscuring effect of the induced dipole seems to be more “drastic” than in the magnetohydrodynamic model of Blöcker et al. (2016), see section 3.3 in that work. Using the same upstream magnetic field as our model, these authors found that inclusion of the dipole mainly causes quantitative changes in the flow deflection pattern, but the local enhancements generated by the plume are still clearly discernible.

3.5. Magnetic Field Analysis Along Hypothetical Spacecraft Trajectories

Figures 6a–6c show all three magnetic field components B_x , B_y , and B_z along hypothetical trajectories through the plumes for Scenarios “.1” to “.4” and a scenario without a plume “JA,” considering only the plasma interaction with a symmetric ($A = 0$) global atmosphere. This setup is similar to the one used by Blöcker et al. (2016), thereby facilitating a direct comparison of the results from both studies. The hypothetical flyby trajectories discussed in this section are displayed in Figure 1. Modeled magnetic field data for a plume located at the south pole (see Figure 6a) are obtained along a trajectory where x changes, $y = 0$, and $z = -1.3 R_E$. For the plume located at Europa’s upstream apex, modeled magnetic field data (see Figure 6b) is shown along a trajectory where z varies, $x = -1.3 R_E$, and $y = 0$. Finally, modeled magnetic field data for a passage through a downstream plume (see Figure 6c) are shown along a trajectory where z changes, $x = 1.3 R_E$ and $y = 0$. At higher altitudes, the magnetic signatures of the plumes quickly faint and become indiscernible from the signatures of the atmospheric interaction. This may be one of the reasons that Galileo detected signatures of plumes only during E12 and E26.

In panel 6a we display the magnetic signatures generated by a plume located at Europa’s south pole. The perturbations in B_x near closest approach are weakest for Case “S.1” (no global atmosphere, just a plume), whereas in the other four cases the draping in B_x is of similar magnitude. The draping signature in B_x , for Cases “S.2” to “S.4” and “JA,” is associated with the crossing of the southern Alfvén wing. Without a plume (Case “JA,” black line), a single, broad enhancement is visible in B_x , whereas the inclusion of a plume generates an “M-like” drop in the strength of the draping near closest approach, similar to observations from the E26 Galileo flyby (see Arnold et al., 2019). The shape of this feature is qualitatively similar in Cases “.2” to “.4,” while the magnitude of the perturbation depends on the chosen atmosphere model and whether the dipole is included. The magnitude of the B_x perturbations is slightly stronger for the case with a dipole included (dashed red line in Figure 6, also shown in Figure 5a). In agreement with Arnold et al.

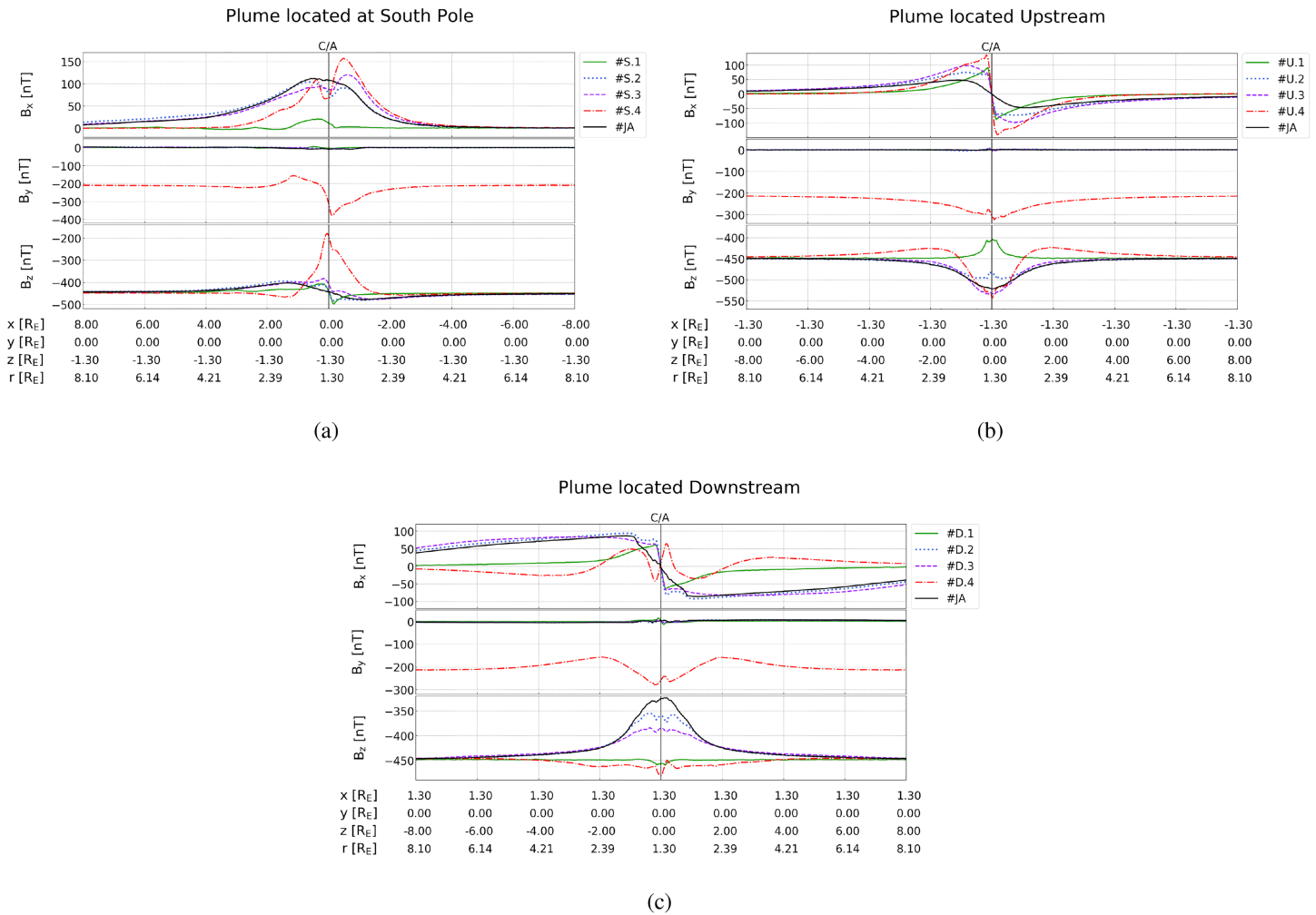


Figure 6. Modeled magnetic field along hypothetical flyby trajectories, as displayed in Figure 1. Each panel displays the field perturbations for a scenario without a plume “JA” and scenarios with a specific plume location: (a) a plume located at Europa’s south pole, (b) a plume located at Europa’s upstream apex, and (c) a plume located at Europa’s downstream apex. Figure 1 shows the geometries for each of the three hypothetical flybys considered here. In that figure, the geometry of panel (a) is represented by the blue line, panel (b) by the red line, and panel (c) by the green line. Each hypothetical trajectory has a closest approach altitude of $0.3 R_E$, similar to the Galileo E12 and E26 flybys where magnetic signatures of plumes were actually observed at Europa.

(2019), there are only very weak signatures of the plumes near closest approach in B_y . This finding is indeed independent of the location of the plume; see Figures 6a–6c. In the case with a Dipole “4,” the y component of the magnetic background field differs from the other runs ($B_{y,0} = -210$ nT instead of $B_{y,0} = 0$ nT). Near closest approach $|B_y|$ displays a bipolar perturbation due to the presence of Europa’s induced dipole. The perturbation signature in B_z is most prominent when a dipole is included (Case “S.4,” the red dash-dotted line). The dipole pushes the pileup region so far toward upstream that in this case (and only in this case) the spacecraft passes through the magnetic depletion region downstream of the enhanced field. The signature of the induced dipole in B_z is much broader and more prominent than any signature associated with the plume; see also Figure 2c of Arnold et al. (2019).

For the flyby upstream of Europa, shown in Figure 6b, the trajectory intersects both Alfvén wings. The perturbation in B_x therefore is positive in Europa’s southern hemisphere ($z < 0$) and negative in Europa’s northern hemisphere ($z > 0$). In the case without a plume (“JA,” black line), a smooth transition between both Alfvén wings can be seen, whereas the inclusion of a plume amplifies the B_x perturbations near closest approach and generates a sharp, discontinuity-like transition from the southern to the northern wing. Due to the C/A altitude of ≈ 460 km, the flyby occurs upstream of Europa’s atmosphere (scale height 100 km); that is, the trajectory intersects the compact Alfvén winglet generated by the plume and not the “main” Alfvén wing, which leads to the sharp transition seen in the B_x component. Looking at B_z , for cases with a symmetric

atmosphere (“U.2”) and a plume only (“U.1”), the plume source pushes the pileup region away from Europa’s surface; that is, the pileup is above the closest approach altitude and the field along the trajectory is slightly reduced. In Scenario “U.3,” the surface density of the neutral atmosphere is 1 order of magnitude larger at Europa’s ramside than at the wakeside and comparable to the surface density of the plume source ($\alpha = 0^\circ$: global atmosphere with $5 \cdot 10^{12} \text{ m}^{-3}$ and plume with $1.6 \cdot 10^{13} \text{ m}^{-3}$). Therefore, the plume is not visible in the pileup structure around C/A of “U.3” (violet dashed line) anymore. A similarly strong pileup is visible in the case of a plume combined with an asymmetric atmosphere and the dipole included (Case “U.4,” red dashed dotted line in Figure 6b), where the dipole again dominates the signature and the plume only causes a very weak kink outbound of C/A.

In Figure 6c, the magnetic field perturbations for a plume located at Europa’s wakeside apex are shown. Similar to the scenarios of Figure 6b (a plume located upstream), the plume generates characteristic fine structures in B_x near closest approach that are not present without a plume (Run “JA,” black line). Again, in Cases “.1” to “.3” (with a plume, without a dipole) a sharp transition between the northern and southern wings is visible around C/A due to the passage through the Alfvén winglet caused by the plume. In the scenario with a dipole included (“D.4,” red dash-dotted line in Figure 6c), the Alfvén wings envelop the quasi-dipolar “shamrock leaf” structure in Europa’s wake: in the southern hemisphere ($z < 0$), the perturbation of B_x is positive for the southern Alfvén wing, whereas the adjacent dipolar contribution is negative (and the other way around for Europa’s northern hemisphere). This scenario is similar to observations of Callisto’s wake during the Galileo C10 flyby (see Liuzzo et al., 2016).

In the scenario without a global atmosphere, Case “D.1” (green line), a weak enhancement is visible in $|B_z|$, caused by plasma absorption at Europa’s surface and deceleration of field lines by the slow plume plasma. The flyby in Scenario “D.1” crossed a small region in between the pileup of the magnetic field and the depletion region (see Figure 2e). Therefore, Case “D.1” shows almost no perturbations in B_z , even though shifting the trajectory by $\approx 0.1 R_E$ in x direction would reveal the pileup structure much more clearly (again, see Figure 2e). This case is a chosen example for the sensitivity of the detectability of plume signatures in magnetic field data, due to chosen flyby geometries. When the global atmosphere is included, the wakeside field B_z is reduced due to the flow deflection around the Alfvén wings, being strongest in the case of just an atmosphere (“JA,” black line). The other cases (“D.2” to “D.4”) reveal the presence of the plume in the form of a wiggly structure near C/A of similar magnitude. This feature is superimposed on the B_z signature generated by the global atmosphere, being weakest for Case “D.3” (purple dashed line) and strongest for “D.4” (red dash-dotted line).

4. Summary and Concluding Remarks

In this study, we have applied the three-dimensional hybrid simulation code AIKEF to investigate the effect of inhomogeneities in Europa’s atmosphere (plumes) on the plasma interaction with the Jovian magnetosphere. To systematically assess the magnitude and structure of the perturbations associated with the plume-plasma interaction, we considered three locations of the plume source at Europa’s surface: Europa’s south pole and the apices of its upstream and downstream hemispheres. These local plume sources have been combined with different symmetric and asymmetric density profiles (taken from Arnold et al., 2019) of Europa’s global atmosphere. To isolate the impact of a plume on Europa’s magnetospheric environment, we also conducted a series of runs without any global atmosphere.

Runs with a plume at Europa’s ramside apex showed highly confined regions ($\approx 1.5 R_E$ in length and width) of water ions upstream of Europa. No pick-up tail in Europa’s wakeside hemisphere is visible because the ions immediately reencounter Europa’s surface and are unable to gyrate around the moon. The reason for the absence of a pick-up tail in this case is the small extent of the plume, compared to the size of the moon, which is a major difference to the Enceladus plume. For a plume located at Europa’s south pole, a complex, filamented fine structure forms in the plume’s pick-up tail. For a plume located at Europa’s downstream apex, a narrow, almost ray-like pick-up tail of plume ions forms along the corotation direction.

At a distance below 400 km to Europa’s surface, the induced dipole from Europa’s subsurface ocean dominates the magnetic field perturbations. Hence, when the dipole is included, the magnetic signatures of a plume will be close to the detection threshold. Flybys close to the center of Jupiter’s magnetospheric plasma sheet, where the horizontal component of the background field is weak (resulting in a weak induced dipole

Zimmer et al., 2000) are therefore most suitable for plume detection through in situ magnetic field and plasma observations.

The magnetic signatures of a plume are best visible in the (hypothetical) case without a global atmosphere. In this case, the plume generates an Alfvén wing with a pronounced north-south asymmetry. Taking into account the plasma interaction of Europa’s global ionosphere severely complicates plume identification. While the plume still generates an Alfvén winglet superimposed on the main wing (see also Blöcker et al., 2016), its visibility is determined by the ratio of the plume’s density and the atmospheric density around the plume location. Our model shows that in the case of an asymmetric atmosphere (denser at Europa’s ram-side by a factor of 10), the signatures of a plume at the ramside apex are almost indiscernible. Irrespective of their location, plumes locally modify the draping signatures in B_x and generate distinct pileup features in B_z , but remain almost “invisible” in B_y . The plasma quantity most diagnostic for the crossing of a plume is the bulk velocity $|\vec{U}|$, which is reduced within a radius of several R_E around the plume source. Overall, precise knowledge of the plasma’s upstream parameters and the density profile of Europa’s global atmosphere is required to identify plumes in plasma data. The detectability of their signatures depends highly on the spacecraft’s trajectory.

Acknowledgments

The authors are grateful to the National Aeronautics and Space Administration (NASA) for financial support of this project through the *Solar System Workings 2016* program, Grant 80NSSC17K0772. Results from the AIKEF hybrid model and figures presented in this publication can be downloaded online (<https://doi.org/10.5281/zenodo.3385994>). The columns of the text files with magnetic field data along a trajectory are structured as follows: $x[R_E]$, $y[R_E]$, $z[R_E]$, $r[R_E]$, $B_x[|B_0|]$, $B_y[|B_0|]$, $B_z[|B_0|]$ and $|\vec{B}[|B_0|]$ with B_0 from Table 1. The binary files in this data repository can be opened using the open-source VisIt software, available online (<https://wci.llnl.gov/simulation/computer-codes/visit/>). The authors would like to thank both referees for careful inspection of the manuscript and for valuable comments.

References

- Arnold, H., Liuzzo, L., & Simon, S. (2019). Magnetic signatures of a plume at Europa during the Galileo e26 flyby. *Geophysical Research Letters*, *46*, 1149–1157. <https://doi.org/10.1029/2018GL081544>
- Bagenal, F., Sidrow, E., Wilson, R. J., Cassidy, T. A., Dols, V., Crary, F. J., et al. (2015). Plasma conditions at Europa’s orbit. *Icarus*, *261*, 1–13. <https://doi.org/10.1016/j.icarus.2015.07.036>
- Blöcker, A., Saur, J., & Roth, L. (2016). Europa’s plasma interaction with an inhomogeneous atmosphere: Development of Alfvén winglets within the Alfvén wings. *Journal of Geophysical Research: Space Physics*, *121*, 9794–9828. <https://doi.org/10.1002/2016JA022479>
- Breer, B. R., Liuzzo, L., Arnold, H., Andersson, P. N., & Simon, S. (2019). Energetic ion dynamics in the perturbed electromagnetic fields near Europa. *Journal of Geophysical Research: Space Physics*, *124*, 7592–7613. <https://doi.org/10.1029/2019JA027147>
- Burger, M. H., & Johnson, R. E. (2004). Europa’s neutral cloud: Morphology and comparisons to Io. *Icarus*, *171*, 557–560. <https://doi.org/10.1016/j.icarus.2004.06.014>
- Cassidy, T. A., Paranicas, C. P., Shirley, J. H., Dalton, J. B. III, Teolis, B. D., Johnson, R. E., et al. (2013). Magnetospheric ion sputtering and water ice grain size at Europa. *Planetary and Space Science*, *77*, 64–73. <https://doi.org/10.1016/j.pss.2012.07.008>
- Coates, A. J., Wellbrock, A., Lewis, G. R., Arridge, C. S., Crary, F. J., Young, D. T., et al. (2012). Cassini in Titans tail: CAPS observations of plasma escape. *Journal of Geophysical Research*, *117*, A05324. <https://doi.org/10.1029/2012JA017595>
- Desai, R. T., Cowee, M. M., Wei, H., Fu, X., Gary, S. P., Volwerk, M., & Coates, A. J. (2017). Hybrid simulations of positively and negatively charged pickup ions and cyclotron wave generation at Europa. *Journal of Geophysical Research: Space Physics*, *122*, 10,408–10,420. <https://doi.org/10.1002/2017JA024479>
- Feyerabend, M., Simon, S., Motschmann, U., & Liuzzo, L. (2015). Filamented ion tail structures at Titan: A hybrid simulation study. *Planetary and Space Science*, *117*, 362–376. <https://doi.org/10.1016/j.pss.2015.07.008>
- Feyerabend, M., Simon, S., Neubauer, F. M., Motschmann, U., Bertucci, C., Edberg, N. J. T., et al. (2016). Hybrid simulation of Titans interaction with the supersonic solar wind during Cassini’s T96 flyby. *Geophysical Research Letters*, *43*, 35–42. <https://doi.org/10.1002/2015GL066848>
- Hall, D. T., Strobel, D. F., Feldman, P. D., McGrath, M. A., & Weaver, H. A. (1995). Detection of an oxygen atmosphere on Jupiter’s moon Europa. *Nature*, *373*, 677–679. <https://doi.org/10.1038/373677a0>
- Ip, W.-H., Williams, D., McEntire, R., & Mauk, B. (1998). Ion sputtering and surface erosion at Europa. *Geophysical Research Letters*, *25*(6), 829–832. <https://doi.org/10.1029/98GL00472>
- Jia, X., Kivelson, M. G., Khurana, K. K., & Kurth, W. S. (2018). Evidence of a plume on Europa from Galileo magnetic and plasma wave signatures. *Nature Astronomy*, *2*, 459–464. <https://doi.org/10.1038/s41550-018-0450-z>
- Kivelson, M. G., Bagenal, F., Kurth, W. S., Neubauer, F. M., Paranicas, C., & Saur, J. (2004). Magnetospheric interactions with satellites. In F. Bagenal, T. E. Dowling, & W. B. McKinnon (Eds.), *Jupiter: The planet, satellites and magnetosphere* (pp. 513–536). Cambridge University Press.
- Kivelson, M. G., Khurana, K. K., Stevenson, D. J., Bennett, L., Joy, S., Russell, C. T., et al. (1999). Europa and Callisto: Induced or intrinsic fields in a periodically varying plasma environment. *Journal of Geophysical Research*, *104*(A3), 4609–4626. <https://doi.org/10.1029/1998JA900095>
- Kivelson, M. G., Khurana, K. K., & Volwerk, M. (2009). Europa’s interaction with the Jovian magnetosphere. In R. T. Pappalardo, W. B. McKinnon, & K. K. Khurana (Eds.), *Europa; with the assistance of René Dotson with 85 collaborating authors, The University of Arizona space science series* (p. 545). Tucson: University of Arizona Press.
- Kriegel, H., Simon, S., Meier, P., Motschmann, U., Saur, J., Wennmacher, A., et al. (2014). Ion densities and magnetic signatures of dust pick-up at Enceladus. *Journal of Geophysical Research: Space Physics*, *119*, 2740–2774. <https://doi.org/10.1002/2013JA019440>
- Kriegel, H., Simon, S., Motschmann, U., Saur, J., Neubauer, F., Persoon, A., et al. (2011). Influence of negatively charged plume grains on the structure of Enceladus Alfvén wings: Hybrid simulations versus Cassini magnetometer data. *Journal of Geophysical Research*, *116*, A10223. <https://doi.org/10.1029/2011JA016842>
- Kriegel, H., Simon, S., Müller, J., Motschmann, U., Saur, J., Glassmeier, K.-H., & Dougherty, M. (2009). The plasma interaction of Enceladus: 3D hybrid simulations and comparison with Cassini MAG data. *Planetary and Space Science*, *57*(14), 2113–2122. <https://doi.org/10.1016/j.pss.2009.09.025>
- Kurth, W., Burnett, D., Persoon, A., Roux, A., Bolton, S., & Alexander, C. (2001). The plasma wave environment of Europa. *Planetary and Space Science*, *49*(3), 345–363. [https://doi.org/10.1016/S0032-0633\(00\)00156-2](https://doi.org/10.1016/S0032-0633(00)00156-2)

- Liuzzo, L., Feyerabend, M., Simon, S., & Motschmann, U. (2015). The impact of Callistos atmosphere on its plasma interaction with the Jovian magnetosphere. *Journal of Geophysical Research: Space Physics*, *120*, 9401–9427. <https://doi.org/10.1002/2015JA021792>
- Liuzzo, L., Simon, S., & Feyerabend, M. (2018). Observability of Callistos inductive signature during the JUPITER ICy Moons Explorer mission. *Journal of Geophysical Research: Space Physics*, *123*, 9045–9054. <https://doi.org/10.1029/2018JA025951>
- Liuzzo, L., Simon, S., Feyerabend, M., & Motschmann, U. (2016). Disentangling plasma interaction and induction signatures at Callisto: The Galileo C10 flyby. *Journal of Geophysical Research: Space Physics*, *121*, 8677–8694. <https://doi.org/10.1002/2016JA023236>
- Liuzzo, L., Simon, S., Feyerabend, M., & Motschmann, U. (2017). Magnetic signatures of plasma interaction and induction at Callisto: The Galileo c21, c22, c23, and c30 flybys. *Journal of Geophysical Research: Space Physics*, *122*, 7364–7386. <https://doi.org/10.1002/2017JA024303>
- McGrath, M. A., Hansen, C. J., & Hendrix, A. R. (2009). Observations of Europa's tenuous atmosphere. In R. T. Pappalardo, W. B. McKinnon, & K. K. Khurana (Eds.), *Europa; with the assistance of René Dotson with 85 collaborating authors, The University of Arizona space science series* (p.485). Tucson: University of Arizona Press.
- Müller, J., Simon, S., Motschmann, U., Schüle, J., Glassmeier, K., & Pringle, G. J. (2011). A.I.K.E.F.: Adaptive hybrid model for space plasma simulations. *Computer Physics Communications*, *182*(4), 946–966. <https://doi.org/10.1016/j.cpc.2010.12.033>
- Müller, J., Simon, S., Wang, Y.-C., Motschmann, U., Heyner, D., Schüle, J., et al. (2012). Origin of Mercurys double magnetopause: 3D hybrid simulation study with A.I.K.E.F. *Icarus*, *218*(1), 666–687. <https://doi.org/10.1016/j.icarus.2011.12.028>
- Neubauer, F. M. (1980). Nonlinear standing Alfvén wave current system at Io—Theory. *Journal of Geophysical Research*, *85*, 1171–1178. <https://doi.org/10.1029/JA085iA03p01171>
- Neubauer, F. M. (1998). The sub-Alfvénic interaction of the Galilean satellites with the Jovian magnetosphere. *Journal of Geophysical Research*, *103*, 19,843–19,866. <https://doi.org/10.1029/97JE03370>
- Neubauer, F. M. (1999). Alfvén wings and electromagnetic induction in the interiors: Europa and Callisto. *Journal of Geophysical Research*, *104*, 28,671–28,684. <https://doi.org/10.1029/1999JA900217>
- Plainaki, C., Cassidy, T. A., Shematovich, V. I., Milillo, A., Wurz, P., Vorburger, A., et al. (2018). Towards a global unified model of Europa's tenuous atmosphere. *Space Science Reviews*, *214*(1), 40. <https://doi.org/10.1007/s11214-018-0469-6>
- Pospieszalska, M. K., & Johnson, R. E. (1989). Magnetospheric ion bombardment profiles of satellites-Europa and Dione. *Icarus*, *78*, 1–13. [https://doi.org/10.1016/0019-1035\(89\)90065-1](https://doi.org/10.1016/0019-1035(89)90065-1)
- Roth, L., Saur, J., Retherford, K. D., Strobel, D. F., Feldman, P. D., McGrath, M. A., & Nimmo, F. (2014). Transient water vapor at Europas South Pole. *Science*, *343*(6167), 171–174. <https://doi.org/10.1126/science.1247051>
- Roth, L., Saur, J., Retherford, K. D., Strobel, D. F., Feldman, P. D., McGrath, M. A., et al. (2016). Europas far ultraviolet oxygen aurora from a comprehensive set of HST observations. *Journal of Geophysical Research: Space Physics*, *121*, 2143–2170. <https://doi.org/10.1002/2015JA022073>
- Rubin, M., Jia, X., Altwegg, K., Combi, M. R., Daldorff, L. K. S., Gombosi, T. I., et al. (2015). Self-consistent multifluid MHD simulations of Europas exospheric interaction with Jupiter's magnetosphere. *Journal of Geophysical Research: Space Physics*, *120*, 3503–3524. <https://doi.org/10.1002/2015JA021149>
- Saur, J., Neubauer, F. M., & Schilling, N. (2007). Hemisphere coupling in Enceladus asymmetric plasma interaction. *Journal of Geophysical Research*, *112*, A11209. <https://doi.org/10.1029/2007JA012479>
- Saur, J., Neubauer, F. M., Strobel, D. F., & Summers, M. E. (1999). Three-dimensional plasma simulation of Ios interaction with the Io plasma torus: Asymmetric plasma flow. *Journal of Geophysical Research*, *104*(A11), 25,105–25,126. <https://doi.org/10.1029/1999JA900304>
- Saur, J., Strobel, D. F., & Neubauer, F. M. (1998). Interaction of the Jovian magnetosphere with Europa: Constraints on the neutral atmosphere. *Journal of Geophysical Research*, *103*, 19,947–19,962. <https://doi.org/10.1029/97JE03556>
- Schilling, N., Neubauer, F. M., & Saur, J. (2008). Influence of the internally induced magnetic field on the plasma interaction of Europa. *Journal of Geophysical Research*, *113*, A03203. <https://doi.org/10.1029/2007JA012842>
- Simon, S., Kriegel, H., Saur, J., Wennmacher, A., Neubauer, F. M., Roussos, E., et al. (2012). Analysis of Cassini magnetic field observations over the poles of Rhea. *Journal of Geophysical Research*, *117*, A07211. <https://doi.org/10.1029/2012JA017747>
- Simon, S., Neubauer, F. M., Wennmacher, A., & Dougherty, M. K. (2014). Variability of Titans induced magnetotail: Cassini magnetometer observations. *Journal of Geophysical Research: Space Physics*, *119*, 2024–2037. <https://doi.org/10.1002/2013JA019608>
- Simon, S., Saur, J., Kriegel, H., Neubauer, F., Motschmann, U., & Dougherty, M. (2011). Influence of negatively charged plume grains and hemisphere coupling currents on the structure of Enceladus Alfvén wings: Analytical modelling of Cassini magnetometer observations. *Journal of Geophysical Research*, *116*, A04221. <https://doi.org/10.1029/2010JA016338>
- Smith, E. J., Davis, L. Jr., Jones, D. E., Coleman, P. J. Jr., Colburn, D. S., Dyal, P., et al. (1974). The planetary magnetic field and magnetosphere of Jupiter: Pioneer 10. *Journal of Geophysical Research*, *79*, 3501–3513. <https://doi.org/10.1029/JA079i025p03501>
- Sparks, W. B., Hand, K. P., McGrath, M. A., Bergeron, E., Cracraft, M., & Deustua, S. E. (2016). Probing for evidence of plumes on Europa with HST/STIS. *The Astrophysical Journal*, *829*(2), 121.
- Volwerk, M., Khurana, K., & Kivelson, M. (2007). Europas Alfvén wing: Shrinkage and displacement influenced by an induced magnetic field. *Annales Geophysicae*, *25*(4), 905–914. <https://doi.org/10.5194/angeo-25-905-2007>
- Volwerk, M., Kivelson, M. G., & Khurana, K. K. (2001). Wave activity in Europas wake: Implications for ion pickup. *Journal of Geophysical Research*, *106*, 26,033–26,048. <https://doi.org/10.1029/2000JA000347>
- Zimmer, C., Khurana, K. K., & Kivelson, M. G. (2000). Subsurface oceans on Europa and Callisto: Constraints from Galileo Magnetometer Observations. *Icarus*, *147*(2), 329–347. <https://doi.org/10.1006/icar.2000.6456>